PNAS RESEARCH ARTICLE | BIOPHYSICS AND COMPUTATIONAL BIOLOGY OPEN ACCESS

Nanoscale dynamics of Dynamin 1 helices reveals squeeze-twist deformation mode critical for membrane fission

Yuliang Zhang[a,1], Javier Vera Lillo[b,c,1,2], Mahmoud Shaaban Mohamed Abdelrasoul[a,1,3], Yaqing Wang[a], Pedro Arrasate[b,c], Vadim A. Frolov[b,c,d,4], and Aleksandr Noy[a,e,4]

Affiliations are included on p. 7.

Edited by James Hurley, University of California Berkeley, Berkeley, CA; received December 6, 2023; accepted October 21, 2024

Dynamin 1 (Dyn1) GTPase, a principal driver of membrane fission during synaptic endocytosis, self-assembles into short mechanoactive helices cleaving the necks of endocytic vesicles. While structural information about Dyn1 helix is abundant, little is known about the nanoscale dynamics of the helical scaffolding at the moment of fission, complicating mechanistic understanding of Dyn1 action. To address the role of the helix dynamics in fission, we used High-Speed Atomic Force Microscopy (HS-AFM) and fluorescence microscopy to track and compare the spatiotemporal characteristics of the helices formed by wild-type Dyn1 and its K44A mutant impaired in GTP hydrolysis on minimal lipid membrane templates. In the absence of nucleotide, membrane-bound ^{WT}Dyn1 and ^{K44A}Dyn1 self-assembled into tubular protein scaffolding of similar diameter encaging the lipid bilayer. In both cases, the GTP addition caused scaffold constriction coupled with formation of 20 to 30 nm nanogaps in the protein coverage. While both proteins reached scaffold diameters characteristic for membrane superconstriction causing fission, the fission was detected only with ^{WT}Dyn1. We associated the fission activity with the dynamic evolution of the nanogaps: ^{K44A}Dyn1 gaps were static, while ^{WT}Dyn1 gaps actively evolved via repetitive nonaxisymmetric constriction-bending deformations caused by localized GTP hydrolysis. Modeling of the deformations implicated filament twist as an additional deformation mode which combines with superconstriction to facilitate membrane fission. Our results thus show that the dynamics of the Dyn1 helical scaffold goes beyond radial constriction and involves nonaxisymmetric deformations, where filament twist emerges as a critical driver of membrane fission.

membrane fission | high-speed atomic force microscopy | membrane remodeling | dynamin

Significance

Highly localized and transient membrane deformations driving membrane fission in the cell often elude experimental observation. Here, we used high-speed atomic force microscopy (HS-AFM) to discriminate between membrane deformation modes produced by Dynamin 1 (Dyn1) fission machinery and compared it to its K44A mutant impaired in guanosine 5′-triphosphate (GTP) hydrolysis. We found that Dyn1 orchestrates membrane fission through a combination of radial membrane constriction and filament twist, which was absent with the mutant. HS-AFM imaging revealed that large twist, enabled by local disassembly of Dyn1 scaffold, caused nonaxisymmetric membrane deformations which acted synergistically with radial constriction. These results underscore the importance of dynamic adaptive architecture of the Dyn1 machinery and emphasize the significance of nonaxisymmetric membrane deformation modes in fission.

Dynamin 1 GTPase is an indispensable component of many endocytic processes at the synapse, including ultrafast clathrin-independent endocytosis, where it is primarily responsible for cleavage of the necks of mature endocytic vesicles (1–5). To support extremely fast membrane turnover there, the Dyn1 machinery shall appear and act swiftly, yet at highly controlled manner, assuming an intricate functional design, a subject of much scientific curiosity (6). The machinery is a short Dyn1 helical oligomer that transiently self-assembles on the vesicle neck and uses the energy of GTP hydrolysis to sever this neck (4, 6). Our mechanistic understanding of this action is to a large extent based upon in vitro reconstruction and modeling of the fission reaction (7–13). Purified Dyn1 readily self-assembles into a fully functional helical machinery on very minimalistic lipid membrane templates (4, 6). Structural and functional assays have long established that GTP hydrolysis drives constriction of the helix and the enclosed lipid membrane tube (3, 6, 14). While there is a consensus that constriction reaches a critical point where the tube yields to the augmenting stress (6, 15), recent experimental and theoretical analyses cast doubts on the ability of the radial constriction of the helix to cause fast membrane fission.

While radial constriction can reach a "superconstricted" (SC) state where the curvature stress inside drives spontaneous fission (16–18), this state is metastable and can be very long-living, especially with K44A mutant of Dyn1 impaired in GTP hydrolysis (18–20). Furthermore, the constriction of the helix might be limited by the elastic resistance of the helical filament itself (21). The superconstriction was linked to changes in helical packing and transition from 1- to 2-start helical arrangement, to alleviate the intrinsic filament stresses (17, 21). Topology of this transition requires local breakup of the helix, as indicated by cryo-EM imaging (17, 22). In agreement with this notion, analysis of molecular scale rearrangements of Dyn1 helices revealed that Dyn1 use the energy

[1]Y.Z., J.V.L., and M.S.M.A. contributed equally to this work.

[2]Present address: Institut de Ciencies Fotoniques, The Barcelona Institute of Science and Technology, Castelldefels 08860, Spain.

[3]Present address: Zoology Department, Faculty of Science, Assiut University, Assiut 71516, Egypt.

[4]To whom correspondence may be addressed. Email: vadim.frolov@ehu.es or noy1@llnl.gov.

This article contains supporting information online at https://www.pnas.org/lookup/suppl/doi:10.1073/pnas.2321514121/-/DCSupplemental.

Published November 27, 2024.

of GTP hydrolysis to break the long assemblies into shorter, fission-competent units (8, 11, 16). Importantly, similar minuscule Dyn1 units mediate membrane fission in the cells (23, 24). However, resolving molecular details of such local and fast rearrangements of Dyn1 helix has always been extremely challenging.

High-speed atomic force microscopy (HS-AFM) has emerged as the technique of choice for real-time visualization of the molecular-scale dynamics of dynamins (8, 25, 26). Yet, HS-AFM imaging of Dyn1 helices requires their preassembly and partial immobilization on the surface, with both procedures potentially impairing fission. To reveal and investigate fast local dynamics of Dyn1 scaffolds under such constraints, we performed comparative HS-AFM analyses of the dynamics of protein scaffolds formed by the wild-type Dyn1 (^{WT}Dyn1) and its K44A mutant (^{K44A}Dyn1), where we used the K44A as an artificially slowed reference sample. We also reduced the substrate attachment constraints to facilitate the scaffold rearrangements in the HS-AFM assays and further compared the HS-AFM and the fluorescence microscopy observations. We confirmed that both proteins could produce local superconstriction. Unexpectedly, in both cases, the superconstriction was coupled to formation of nanogaps in the protein scaffold. Quantification of the scaffold deformations at the gaps linked them to local changes of the scaffold geometry during the transition from 1-start to 2-start helical configurations (17, 18). While the nanogaps were the likely hot spots for membrane fission (11, 27), no apparent fission events were detected with ^{K44A}Dyn1, in agreement with previous observations (18). We associated the fission with the large and reversible nonaxisymmetric deformations seen at wide nanogaps detected only in the ^{WT}Dyn1 scaffolds. Such deformations implicated Dyn1 filament twist as a critical addition to superconstriction for effective catalysis of membrane fission (9, 28).

Results

Comparative Analysis of Nanoscale Membrane Constriction by ^{WT}Dyn1 and ^{K44A}Dyn1. To compare ^{WT}Dyn1 and ^{K44A}Dyn1 in action, we resorted to widely used reconstitution strategy where the protein helix initially self-assembles in the nucleotide-free (apo) state, defining the reference membrane geometry, before GTP is added (26, 29). In fluorescence microscopy experiments, we used microns-long lipid membrane nanotubes (NTs) pinned to a planar support (Fig. 1*A* and *SI Appendix*, Fig. S1), the template long used for quantification of membrane constriction and fission (29–31). K44A mutation does not interfere with the helical self-assembly of Dyn1 (16, 18). Addition of ^{K44A}Dyn1-mEGFP (1 μm bulk) to preformed NTs resulted in formation of long cylindrical protein scaffolds (Fig. 1*A*, green) causing the NT constriction, seen as a decrease of lipid fluorescence in the NT parts covered by the scaffolds (Fig. 1*A*, red). GTP addition augmented the constriction, seen as further decrease of the lipid fluorescence intensity (Fig. 1 *A* and *B*). The GTP-induced transformation was slow (22) and variable from scaffold to scaffold: While some scaffolds remained virtually "unconstricted," in others, the constriction continued still 50 min after GTP addition (Fig. 1*B* and *SI Appendix*, Fig. S1*A*). Within a single scaffold, the constriction was also nonuniform (Fig. 1*B* and *SI Appendix*, S1*B*), with the minimal radius ranging from 4 nm (superconstricted Dyn1 helices) to 7 to 8 nm (the partially constricted helices) (17, 22). Despite approaching local SC state, 37 out of 40 NTs covered by ^{K44A}Dyn1-mEGFP scaffolds remained stable 50 min after GTP addition, in agreement with much reduced fission activity of the mutant (18).

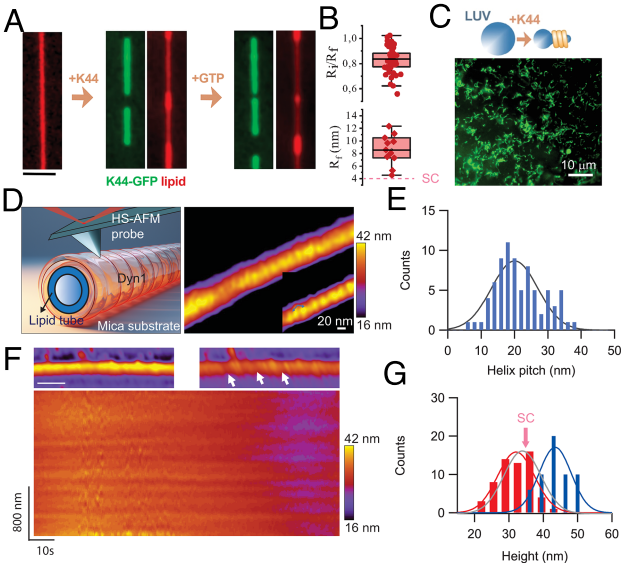

Fig. 1. Nanoscale characterization of geometry and dynamics of GTP-driven constriction of the ^{K44A}Dyn1 scaffold. (*A*) Self-assembly and GTP-driven constriction of ^{K44A}Dyn1-mEGFP scaffolds on preformed lipid nanotubes. ^{K44A}Dyn1-mEGFP (green) and Rh-DOPE lipid marker (red) fluorescence images are shown. (Scale bar: 5 μm.) (*B*) Boxplots show average membrane constriction measured as the ratio of the total Rh-DOPE fluorescence from the membrane nanotube under the scaffold (*SI Appendix*, Fig. S1*B*) obtained 1 s and 30 min after GTP addition (*Upper* box) and the minimal (*SI Appendix*, Fig. S1*B* midplane) radius, measured at the membrane midplane, of the constricted nanotube (*Lower* box). (*C*) ^{K44A}Dyn1-mEGFP scaffolds (green) self-assembling via tubulation (cartoon) of 400 nm large unilamellar vesicles (LUV). (*D*) Illustration of a tubular ^{K44A}Dyn1 scaffold with lipid nanotubes inside deposited on mica surface (*Left*) and HS-AFM image of the scaffold (*Right*). Blue arrows in the *Inset* indicate the distance between the adjacent peaks in the scaffold height. (*E*) The distribution of the peak-to-peak distance measured as shown on panel (*D*) (*Inset*). N = 77, from 4 tubes. (*F*) Kymograph illustrating progressive decrease of the ^{K44A}Dyn1 scaffold height upon GTP addition. The initial and final images of the scaffold are shown above (Scale bar: 200 nm), the arrows point to nanogaps. (*G*) The distribution of the ^{K44A}Dyn1 scaffold height measured at 1 to 10 s (blue, 45.1 ± 4.0 nm, N = 56) and 30 to 50 min (red, 33.8 ± 5.0 nm, N = 59) after GTP addition (as described in *Materials and Methods*); the solid lines are from Gaussian fitting; the arrow indicates the height characteristic of superconstriction (17); the solid gray line is the fit from a simulated Gaussian distribution with a mean of 36 nm (superconstriction value) and a SD of 5.0 nm. A statistical *t* test shows that the mean scaffold size value is similar to the literature value for superconstricted scaffold size ($P = 0.025$).

To obtain higher-resolution insights into the spatiotemporal characteristics of this nonuniform constriction process, we turned to HS-AFM imaging (32, 33). As the membrane templates, we chose large unilamellar vesicles (LUVs) used in cryo-EM analyses of ^{K44A}Dyn1 helices (18, 22). Addition of ^{K44A}Dyn1-mEGFP (2 μm) to the LUVs resulted in massive tubulation of the vesicles: Multiple tubular scaffolds resembling those formed on NTs (Fig. 1*A*) could be resolved by fluorescence microscopy (Fig. 1*C*). These scaffolds were then partially immobilized on a freshly cleaved mica substrate for the HS-AFM scanning (Fig. 1*D* and Movie S1). Individual scaffolds situated parallel to the interface (Fig. 1*D* and *SI Appendix*, S2*A*) were clearly resolved. We focused on the individual submicron (100 to 500 nm in length) scaffolds corresponding to one to several pixels in the fluorescence microscopy images. In the apo state, such scaffolds remained static (*SI Appendix*, Fig. S2*B*, apo kymograph). Their height showed a periodic pattern along the tubular axis, with the peak-to-peak distance of 22.3 ± 7.0 nm (SD, N = 77)

(Fig. 1*E*). While this distance is consistent with the earlier HS-AFM observations of the ^{WT}Dyn1 (25, 26, see also *SI Appendix*, Fig. S2 *C–E*), it is larger than the pitch of the Dyn1 helices analyzed by cryo-EM [around 12 nm, (7)], indicating a looser protein packing on the membrane surface. Indeed, occasional thermal-driven local rearrangements of the scaffold were observed (*SI Appendix*, Figs. S2*C* and S3 and Movie S2). The mean value of the scaffold heights is 45.1 ± 4.0 nm (Fig. 1*G*, blue), slightly smaller than the diameter of Dyn1 helix in the apo state (18), also in agreement with the earlier HS-AFM analysis (25).

Addition of GTP to the performed ^{K44A}Dyn1 scaffolds caused gradual decrease of the height (Fig. 1*F*). The mean value of the height, measured 30 min after GTP application, shifted to 33.8 ± 5.0 nm (Fig. 1*G*, red), slightly below the diameter of the superconstricted ^{K44A}Dyn1 helices (Fig. 1*G*, gray, *t* test, $P = 0.025$) derived from cryo-EM (18) but significantly different from the apo state (Fig. 1*G*, blue, *t* test, $P < 0.001$). The large width of the distribution showed that the constriction was quite nonuniform at the nanoscale (Fig. 1*G* and *SI Appendix*, Fig. S4). The right shoulder of the distribution corresponded to partial constriction seen by fluorescence microscopy (Fig. 1 *B* and *G*). It is plausible that the constriction of ^{K44A}Dyn1 scaffolds was initiated locally and then slowly propagated along the scaffolds, with superconstriction achieved only at the submicron scale 30 min after GTP application (*SI Appendix*, Fig. S1). Importantly, the low height values seen in the extended left shoulder of the distribution indicated that some scaffolds broke locally where the corresponding nanogaps were visible in the HS-AFM images of the scaffolds (Fig. 1*F*, arrow). Such nanogaps have been associated with membrane fission in the earlier HS-AFM studies of ^{WT}Dyn1 (25, 26). However, ^{K44A}Dyn1 scaffolds remained stable when monitored by fluorescence microscopy.

We next compared ^{K44A}Dyn1 and ^{WT}Dyn1 scaffolds in our assays. ^{WT}Dyn1-mEGFP (0.5 μM bulk) formed large scaffolds on the preformed NTs, with GTP addition triggering multiple fission events (Fig. 2*A* and Movie S3). Addition of mEGFP resulted in slightly reduced GTPase activity of the ^{WT}Dyn1 (*SI Appendix*, Fig. S1*C*), yet all of the 25 NTs tested (in 3 independent assays) broke within a few minutes upon GTP application. In contrast, no NT breakage was detected with ^{K44A}Dyn1-mEGFP 30 min after GTP application (N = 40, 3 independent assays). ^{WT}Dyn1-induced fission was followed by membrane retraction to the points of the NT adhesion to the substrate (Fig. 2*A*, green points). In the process, the ^{WT}Dyn1-mEGFP scaffolds first became increasingly shorter (Fig. 2 *B*, arrow and *C* and Movie S4), then transformed to compact globular structures (Fig. 2*B*), consistent with the progressive decrease of the scaffold persistent length by the GTP hydrolysis (11, 34). Similar decrease of the scaffold length upon GTP addition was seen with ^{K44A}Dyn1-mEGFP (Fig. 2*C*). On a single NT the length of multiple scaffolds decreased synchronously, resulting in appearance of large openings between the scaffolds (Fig. 2*A*). The simultaneous crumpling of many scaffolds indicated an elastic stress buildup during the hydrolysis. To resolve these scaffold transformations in more details, we again turned to HS-AFM.

As with ^{K44A}Dyn1 experiments, we used 400 nm LUVs as a membrane substrate to make ^{WT}Dyn1-mEGFP scaffolds immobilized on a mica substrate (*SI Appendix*, Fig. S2 *C–E*) for the HS-AFM scanning (see also refs. 25 and 26). Their height in

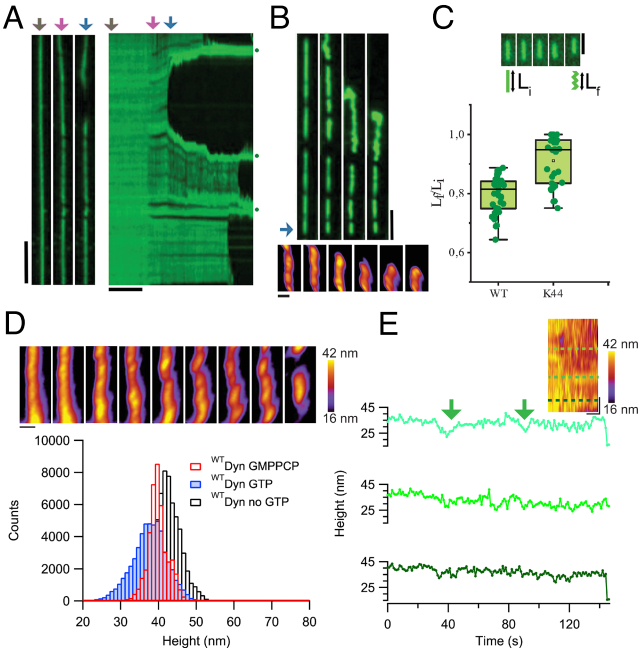

Fig. 2. Complex and reversible changes of the ^{WT}Dyn1 scaffold geometry and connectivity driven by GTP hydrolysis. (*A*) Image sequence and kymograph show fragmentation and fission of ^{WT}Dyn1-mEGFP scaffold (preassembled on an NT) upon GTP addition (at t = 0). The arrows indicate GTP addition (gray), fragmentation (magenta), and fission (blue-green); the dark green points mark the substrate adhesion sites. [Scale bars: 10 s (horizontal) and 10 μm (vertical).] (*B*) Fluorescence microscopy (*Upper*, mEGFP fluorescence is seen, 0.2 s between frames, Scale bar: 5 μm) and HS-AFM (*Lower*, 1 s between frames, Scale bar: 100 nm) image sequences illustrate retraction and globular transformation of ^{WT}Dyn1-mEGFP scaffolds upon membrane fission. The arrow points to a shrinking protein scaffold. (*C*) Image sequence (1 s between frames) shows progressive decrease of the axial length of ^{WT}Dyn1-mEGFP scaffold upon GTP addition; (Scale bar: 5 μm.) The boxplots show the relative decrease of the axial length of the protein scaffold measured prior to the globular transition (^{WT}Dyn1) or 30 min after GTP addition (^{K44A}Dyn1). (*D*) HS-AFM image sequence (4 s between frames, 1 s between the last 2 frames) shows ^{WT}Dyn1-mEGFP scaffold transformations upon GTP addition. The *Lower* panel shows the distribution of the height of ^{WT}Dyn1-mEGFP scaffolds prior to the fission (GTP, blue) in apo state (black) and 5 min upon addition of GMPPCP (red). (Scale bar: 100 nm.) (*E*) Kymograph (Scale bars: 40 s and 100 nm) corresponding to the HS-AFM sequence in panel (*D*) shows the scaffold height changes caused by GTP hydrolysis. The graphs show the height variations along the dash lines on the kymograph, arrows indicate reversible superconstriction.

the apo state was comparable to that measured with ^{K44A}Dyn1 (Fig. 2*D*). Addition of GTP triggered rapid changes of the shape and height of the ^{WT}Dyn1-mEGFP scaffolds (Fig. 2*D*, image row and Movie S5). The scaffold constriction was several times faster than with ^{K44A}Dyn1 (see kymographs Figs. 1*F* and 2*E*) and ended in superconstriction (Fig. 2 *D* and *E*). The height distribution closely resembled that obtained with ^{K44A}Dyn1, with the large left shoulder indicating formation of nanogaps clearly visible in the HS-AFM images (Fig. 2*D*). In stark contrast to ^{K44A}Dyn1, ^{WT}Dyn1-mEGFP scaffolds produced membrane fission events in 21 out of 22 cases 34.4 ± 13.1 s (SD, N = 21) after GTP addition, comparable with the fission times reported by fluorescence microscopy and electrophysiology experiments (16, 29). As in the fluorescence microscopy experiments, fission resulted in the retraction of the scaffold parts toward the adhesion points (Fig. 2 *B*, *Lower* panel and Movie S6). Crucially, retraction enabled us to discriminate complete fission from stable nanogaps formation in the protein scaffold: The nanogaps forming in ^{K44A}Dyn1 scaffolds are unlikely to

indicate fission, in agreement with the fluorescence microscopy observations.

Importantly, the nanogaps emerged during superconstriction of the ^{WT}Dyn1 scaffolds but not during their partial constriction induced by nonhydrolyzable GTP analogue βγ-Methyleneguanosine 5′-triphosphate (GMPPCP) (17, 35): 5 min after GMPPCP addition, the scaffold heights remained above the superconstriction limit (Fig. 2 *D*, red and Movie S7). The edges of a superconstricted Dyn1 scaffold have long been considered hotspots of membrane fission (6, 27). Then the coordinated appearance of the gaps and superconstriction upon GTP hydrolysis shall make the membranes primed for spontaneous fission in both ^{WT}Dyn1 and ^{K44A}Dyn1 experiments. Visual inspection associated the fission deficiency of ^{K44A}Dyn1 with much slowed membrane dynamics at the points of membrane constriction and nanogap formation. In the ^{K44A}Dyn1 scaffolds, the nanogaps remained static and rarely changed their shape or their orientation (Fig. 1*F* and Movie S8). In the ^{WT}Dyn1 scaffold acute drops of the scaffold height, indicative of a nanogap formation, were initially transient and randomly distributed along the scaffold (Fig. 2*E*). Such transient and repetitive superconstriction events (e.g. Fig. 2*E*, arrows) evoke membrane curvature oscillations produced by short ^{WT}Dyn1 scaffolds (11). With time, this activity resulted in larger and more prolonged membrane constriction, concurring with visible bending deformations of the scaffold axis (Fig. 2*D*). Interestingly, such zig-zags deformations could account for the macroscopic decrease of the scaffold length seen in fluorescence microscopy experiments (Fig. 2 *B* and *C*). We next analyzed these nonaxisymmetric scaffold deformations.

Nanoscale Breakups Coupled to Local Bending Indicate Transformation of ^{WT}Dyn1 Scaffold into 2-Start Helix for Superconstriction. We began from quantifying the bending of the scaffold axis as the curvature of the line approximating the height peaks of the protein scaffold (Fig. 3*A*, rainbow line). Initial distribution of this axial curvature was variable, biased by adhesion to the substrate. We then used the maximum curvature as a simplified metrics of the scaffold deformations appearing upon the nucleotide addition. GTP drove the maximum curvature of ^{WT}Dyn1 scaffolds significantly higher than GMPPCP (Fig. 3*B*), while ^{K44A}Dyn1 scaffolds showed intermediate maximal curvature values. Lesser axial bending could also account for smaller decrease of the ^{K44A}Dyn1 scaffold length seen by fluorescence microscopy (Fig. 2*C*).

Both the axial curvature and the local height of ^{WT}Dyn1 scaffolds showed large-scale reversible changes (Figs. 2*E* and 3 *C*, *Inset*). We tested whether these changes were correlated and indeed observed that the average magnitude of local axial curvature increased dramatically with the scaffold constriction (Fig. 3*C*). The mean value of the maximal curvature, 0.05 nm^{-1} (Fig. 3*B*), sets the characteristic length of the bending deformation, 20 nm. This value was comparable to the length of a 2-rung Dyn1 helix, which is the minimal helical unit capable of stimulated GTP hydrolysis (4, 11, 17). Hence, it seemed plausible that the constriction-bending deformations of the protein scaffolds seen here were driven by localized bursts of GTP hydrolysis randomly distributed along the scaffolds (36, 37). The deformations then could be rationalized by a minimalistic model of the local transitions of Dyn1 scaffold between 1-start to 2-start helical arrangements predicted by cryo-EM analysis (17, 21, 22). The GTP hydrolysis, initiated by dimerization between the GTPase (G) domains of Dyn1 in the adjacent helical rungs, drives the

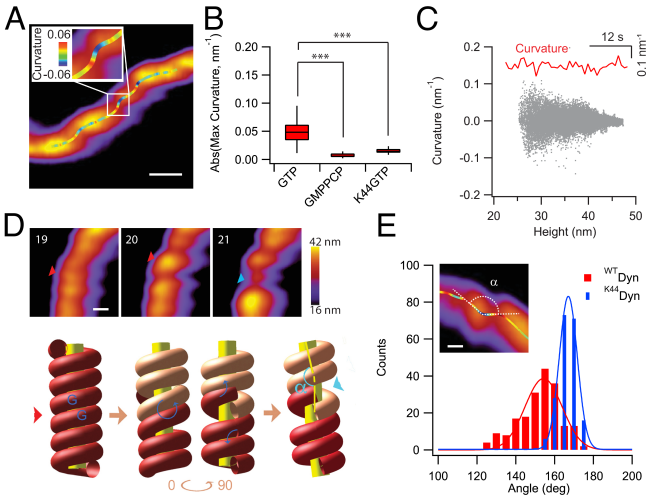

Fig. 3. HS-AFM quantification and modeling of the deformations and breakup of the ^{WT}Dyn1 scaffold driven by localized GTP hydrolysis. (*A*) HS-AFM image of characteristic zig-zag bending deformations of the ^{WT}Dyn1 scaffold appearing 11 s after GTP addition. The insert shows changes of the curvature of the line approximating the peak height of the scaffolds (rainbow line). (Scale bar is 100 nm.) (*B*) The boxplot showing the maximal curvatures measured as described in panel A (GTP, N = 329 from 17 tubes; GMPPCP, N = 276 from 3 tubes. K44, N = 480 from 3 tubes, *** indicates significant difference (Kolmogorov–Smirnov test, $P < 0.001$). (*C*) Variations of the axial curvature caused by GTP hydrolysis intensify with the decrease of the ^{WT}Dyn1 scaffold height. The *Inset* shows a representative example of the scaffold curvature changes with time. (*D*) HS-AFM image sequence (*Above*) and the cartoon (*Below*) show a local breakup of ^{WT}Dyn1 scaffold (cyan arrow) due to localized structural rearrangements of the scaffold (red arrows) caused by GTP hydrolysis. (Scale bar is 50 nm.) The cartoon shows how the hydrolysis-driven transition of the two rungs (marked by GG) of Dyn1 helix from 1-start (red) to 2-start (red and tan) configuration leads to the scaffold breakup and bending of its axis (yellow line), parameterized by the bending angle α. (*E*) The distributions of the bending angle obtained from HS-AFM images (as shown in the *Inset*) for ^{WT}Dyn1 scaffolds (red) and ^{K44A}Dyn1 scaffold (blue). Solid lines correspond to the Gaussain fits to the data. (Scale bar is 50 nm.)

transformation seen as local constriction of the helix coupled to the increase of the pitch (17, 35, 38) and helical angle (defined here as $\alpha_h = \arctan(p/2d)$, where p and d are the pitch and diameter of the helix respectively, Fig. 3*D*). The associated torque (Fig. 3*D*, blue arrow) results in the scaffold breakup (Fig. 3*D*, cyan arrows) (17). An instant appearance, followed by tilting, of a small distinct part of the ^{WT}Dyn1 scaffold can be detected prior to the local breakup of the scaffold (Fig. 3*D*, the HS-AFM image sequence, Movie S9).

During the breakup, the emergent 2-start helical insert pushes away the initial 1-start helix (Fig. 3*D*, blue arrows) thus causing axial bending (Fig. 3*D*, yellow lines). If the 2-start insert remains continuous with the 1-start background helix, the bending angle α is defined by the difference between the helical angles of 1- and 2-start Dyn1 helices ($\Delta\alpha = \alpha_{2h} - \alpha_{1h}$) as $\alpha = 180° - \Delta\alpha$. To test this conjecture experimentally, we measured the bending angle distribution using the peak height line defined above (Fig. 3 *A* and *E*, *Inset*) and compared it with the calculated value of 170° obtained with $P = 13$ nm and d = 52 nm for α_{1h} (17, 35) and $P = 20$ nm and d = 36 nm for α_{2h} (17). Remarkably, the mean α (169.2 ± 4.5°) of ^{K44A}Dyn1 scaffolds was statistically undistinguishable (t test, P = 0.088) from 170° (Fig. 3*E*). This angle corresponded to relatively small value of the axial curvatures seen with ^{K44A}Dyn1 (Fig. 3*B*). Hence, the GTP-driven nonaxisymmetric bending deformations of ^{K44A}Dyn1 scaffolds were limited, causing local breakups of the scaffolds enabling slow development of membrane superconstriction, yet

not sufficient for effective catalysis of membrane fission (Fig. 3 *B* and *E*). In turn, smaller α (154.6 ± 10.9°, *t* test, $P < 0.001$) corresponding to larger curvature values were measured with ^{WT}Dyn1 (Fig. 3 *B* and *E*). We next explored the link between large local deformations seen with ^{WT}Dyn1 scaffolds and fission.

Large Nonaxisymmetric Deformations of WT Scaffold Implicate Filament Twist in the Scaffold Fragmentation and Membrane Fission. This link is the most evident in the evolution of the ^{WT}Dyn1 scaffolds upon the GTP addition. Following our model (Fig. 3*D*), we could discriminate several distinct stages of the scaffold transformations, from the appearance of the initial stress patterns to scaffold breakups and fission (marked by arrows in Fig. 4*A* and Movie S10). No fission has been detected prior to the nanogap opening despite the prolonged period of the scaffold rearrangements: Fission always (in 21 out of 22 cases) happened at a nanogap. Furthermore, acute axial bending deformations associated with the nanogap opening could also be detected right before fission (Fig. 4*B*). Dynamic coupling to the local constriction of the scaffold (Fig. 3*C*), as well as fast and reversible character of such deformations (Fig. 4 *B* and *D*), all indicate that they, as the initial scaffold breakups, are driven by the local GTP hydrolysis. Correspondingly, substantial changes in curvature were also observed at the limit of our time resolution for HS-AFM studies, one frame prior to fission (Fig. 4*C*, $\Delta k = 0.06 \pm 0.02$ nm^{-1}, SD, N = 7).

To explain how the hydrolysis-driven deformations of ^{WT}Dyn1 scaffold go beyond the local changes of helical geometry (seen in Fig. 3*D*), we evoked filament twist long implicated in Dyn1 membrane remodeling (7, 9). The twist (Fig. 4*E*, blue arrows) accompanies changes of the helical geometry (17), yet its action on the membrane is constrained by the protein scaffold. However, when the breakup in the scaffold approaches the diameter of the lipid membrane tube inside of scaffold (10 to 20 nm, Fig. 1*B*), the tube can wind around the filament during its twisting motion (Fig. 4*E*, yellow arrows), as previously reported (28, 39). The corresponding zig-zag height pattern is clearly seen in the HS-AFM images of ^{WT}Dyn1 scaffold 20 to 30 s after GTP addition (Fig. 4*D*, arrow). The changes of the local orientation of the scaffold axis can be large (Fig. 4*E*, dashed lines), explaining macroscopic contraction of ^{WT}Dyn1 scaffolds (Fig. 2*E* and 4 *B* and *D*). Even stronger twist might cause further compactization of the scaffolds into globular structures seen at the end of the scaffold retraction upon fission (Fig. 2 *A* and *B*).

Neither the zig-zag scaffold deformations nor their retraction upon fission was detected in earlier HS-AFM analyses of ^{WT}Dyn1-driven membrane fission. We attributed this discrepancy to the density of the substrate adhesion points, which was smaller in our assays. Looser adhesion, while undoubtedly complicating the HS-AFM imaging, enables higher degree of freedom for the protein scaffold transformations. If the scaffold is pinned to the substrate only at one point, the twist action generated from this fixed point might move the whole scaffold. We indeed detected such macroscopic twist-like deformations with the ^{WT}Dyn1-mEGFP scaffolds attached to the substrate at one end (Fig. 4*F* and Movie S11). The large twist angle and the fast timing (ca. 100 ms) of the twist closely resembled the supertwist Dyn1 action resolved in cells expressing the protein [Fig. 4*F*, (40)]. Overall, these results identify filament twist occurring only at large nanogaps in the ^{WT}Dyn1 scaffolds as additional catalytic element facilitating membrane fission in these already highly constricted membrane sites.

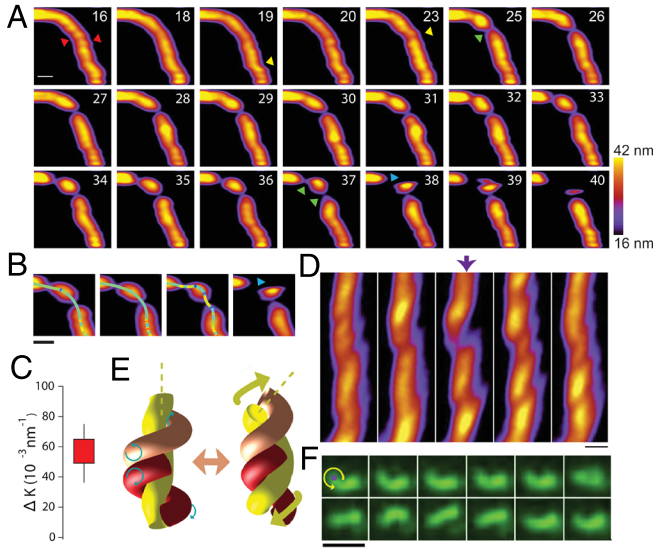

Fig. 4. Twist of the ^{WT}Dyn1 filament in nonaxisymmetric membrane deformations and fission. (*A*) HS-AFM image sequence (with frame time in seconds indicated on each frame) illustrating the sequence of structural rearrangements of a ^{WT}Dyn1 scaffold upon GTP addition. Arrows highlight appearance of strain patterns (red arrows), axial bending (yellow arrows), nanogaps (green arrows), and membrane fission (cyan arrow). (Scale bar: 100 nm.) (*B*) Zoom-in of the image sequence in panel (*A*) reveals large local deformations of the scaffold axis (rainbow line) prior to fission (cyan arrow). (Scale bar: 100 nm.) (*C*) Curvature changes prior to (1 frame before) fission. (*D*) HS-AFM image sequence shows large and transient local bending of the ^{WT}Dyn1 scaffold (arrow). (Scale bar: 100 nm.) (*E*) A model of the large twist-like deformation of ^{WT}Dyn1 scaffold (yellow arrows) caused by the protein filament twist (blue arrows). The dash yellow lines illustrate the corresponding bending of the scaffold axis. (*F*) Fluorescence microscopy image sequence (5 fps) of twist-like reversible deformations of ^{WT}Dyn1-mEGFP scaffold pinned at one end (marked by the magenta point) to the planar support. ^{WT}Dyn1-mEGFP fluorescence image is shown, (Scale bar: 5 μm.)

Discussion

Since the discovery of Dyn1 self-assembly into rings and helices, its ability to create high membrane curvatures associated with membrane fission has been confirmed in multiple assays (15, 16, 41, 42). Yet, it has long been understood that the cylindrical constriction produced by long Dyn1 helices is not an optimal path to membrane scission: Local membrane shape is to deviate from the cylinder to minimize the associated energy barriers (11, 15). Researchers proposed that fission can still be triggered near the edges of the helix where the geometry constraints imposed by the helix are relaxed (11, 15, 27, 43). However, as we show here with ^{K44A}Dyn1, appearance of breakups and nanogaps in a superconstricted cylindrical scaffold is not sufficient to trigger rapid membrane fission (Fig. 2*F*), which is also consistent with recent cryo-EM observations (22). Long ^{WT}Dyn1 helices could also be trapped in a metastable superconstricted state [Fig. 2 *D* and *E*, (17)]. Interestingly, other proteins, such as reticulon (36) and endophilin (44), implicated in cellular membrane fission can stabilize cylindrical membrane geometry, with fission requiring an additional constriction factor, such as membrane pulling force (45).

In agreement with the deficiency of the uniform cylindrical constriction in membrane scission, we found that preassembled ^{WT}Dyn1 scaffolds are constricted highly nonuniformly (Fig. 2 *D* and *E*). The constriction is localized to 20 to 30 nm active sites which could be associated with local bursts of GTP hydrolysis (37). The resulting packing frustration causes

nonaxisymmetric zigzag deformations and scaffold breakups prior to fission. Importantly, these deformations reflect relative freedom of the scaffold movement in our assay, also seen in the scaffold retraction upon fission (Fig. 2*B*). Constraining the scaffold more might inhibit these local oscillations and thus fission, plausibly explaining the slow fission rates obtained in earlier HS-AFM experiments (26). While the nanoscale adhesion might affect the scaffold deformations in the HS-AFM assay, microscopic shrinkage of the scaffolds is consistent with nanoscale zigzag deformations (Fig. 2*E*). Thus, while long Dyn1 scaffolds preassembled in apo state remain purely in vitro structures, their local deformations report important properties of the Dyn1 scaffold rearrangements at the physiologically relevant length scale (4, 6, 11).

Quantification of the local constriction of the scaffold and the associated axial bending angle indicates that both ^{WT}Dyn1 and ^{K44A}Dyn1 scaffolds switch from 1-start to 2-start helical configuration for superconstriction [Fig. 3 *C* and *D*, (17, 21)]. Larger local deformations, seen only with ^{WT}Dyn1 scaffolds, could be explained by a filament twist (28). The twist accompanies constriction of the Dyn1 helix (17). Recent studies suggested that such changes might apply torque to the underlying lipid bilayer (8, 9). The torque action might explain how relatively small changes of the helical geometry driven by GTP hydrolysis can lead to large axial bending and even microscopic deformations of the scaffold (Fig. 4 *D* and *E*). The torque is applied via membrane-bound plekstrin-homology domains (PHD) of Dyn1 (8, 9, 11). The PHD swinging can be large (46), driving the membrane tube winding around the Dyn1 helical filament in a wide enough nanogap [Fig. 4*E*, (28, 47)]. Such large twist-like membrane deformation produced by Dyn1 was reported earlier, both in vitro and in the cells expressing Dyn1 (34, 40). As in our system, the cellular twist directly preceded membrane fission and was much faster than the prior membrane deformations [Fig. 4 *D* and *E*, (40)], indicative of a local burst of GTP hydrolysis as the driver.

The filament twist could accelerate fission by different means. In the emerging 2-start helix the movement of PHD in the opposite direction (following the twist indicated by blue circular arrows in Fig. 4*E*) would promote local membrane constriction and scission following the geometric catalysis mechanism (11, 15). The acute torque associated with rapid twisting of the dynamin filament can also augment constriction and/or tensile stresses linked to fission (9, 47). Importantly, the propagation of the twist deformation to macroscale (Fig. 4*E*) implicates the associated torque in the scaffold disassembly and recycling (7, 9, 28). While the mechanisms of the torque generation and spatial distribution need more investigation, our results demonstrate that Dyn1 utilizes the energy of GTP hydrolysis not only for radial membrane constriction but also for acute torque action, which supplements membrane constriction in fast fission coupled with proper disassembly and recycling of the scaffold. These features are crucial for Dyn1 integration with the rest of the protein machinery that enables extremely fast membrane turnover at the synapse.

Materials and Methods

^{WT}Dyn1 and ^{K44A}Dyn1 Protein Purification. ^{WT}Dyn1-mEGFP pIEX6 plasmid, encoding ^{WT}Dyn1 protein conjugated with monomeric enhanced GFP (43), was kindly provided by Dr. Sandra Schmid lab (UT Southwestern, Dallas). K44A mutation was introduced using In—Fusion® HD EcoDry™ Cloning Kit (Takara Bio), following the manufacturer protocol. The proteins were expressed in Sf9 cells and purified using immobilized GST tagged amphiphysin-II SH3 domain as affinity ligand as described earlier (43) in buffer containing 20 mM HEPES (pH 7.2), 150 mM KCl, 1 mM DTT, 1mM EDTA, and 1 mM EGTA. The protein was aliquoted in 5% of glycerol, flash-frozen in liquid nitrogen, and stored at −80 °C. Prior to the experiments, the proteins were transferred to the working buffer (150 mM KCl, 10 mM HEPES, 2 mM $MgCl_2$, 1 mM EGTA, and pH 7.5) using Slide-A-Lyzer MINI Dialysis units (10k MWCO) or ZebaTM spin desalting columns (ThermoFisher Scientific). We have compared ^{WT}Dyn1-mEGFP with unmodified ^{WT}Dyn1 and verified that ^{WT}Dyn1 was also capable of GTP-induced membrane fission in HS-AFM experiments (*SI Appendix*, Fig. S5 and Movie S12).

Lipid Vesicle Preparation. All lipids were purchased from Avanti Polar Lipids and used as received. Lipid vesicles were prepared using 20% 1,2-dioleoyl-snglycero- 3-phospho-L-serine (DOPS), 67.5% 1,2-dioleoyl-sn-glycero-3-phosphocholine (DOPC), 2% L-α-phosphatidylinositol-4,5-bisphosphate (Brain, Porcine) (ammonium salt) (PI(4,5)P2), 10% cholesterol, 0.5% 1,2-dioleoyl-sn-glycero-3-phosphoethanolamine-N-(lissamine rhodamine B sulfonyl) (ammonium salt) (18:1 Liss Rhod PE), mol:mol mixture. Lipids dissolved in chloroform were dried under Ar flux, followed by two hours incubation in a desiccator. Hereafter, lipids were fully rehydrated to 1 mg/ml with GTPase buffer (150 mM KCl, 10 mM HEPES, 2 mM $MgCl_2$, 1 mM EGTA, and 1 mM DTT at pH 7.5) for 10 min at room temperature (RT). Finally, the lipid suspension was vortexed for 10 s and then passed through a 400 nm filter.

HS-AFM Sample Preparation. To form dynamin-lipid assemblies for HS-AFM imaging, lipid vesicles were first tubulated by incubation with ^{WT}Dyn1 or ^{K44A}Dyn1, where 2 μL of lipid vesicle suspension (1 mg/mL) were mixed with 2 μL protein solution (1 μm) and incubated at RT for 10 min. Subsequently, the protein–lipid assemblies were deposited on freshly cleaved mica surface and incubated for 5 min at RT before being rinsed by 20 μL of buffer for 5 times. We found that small amounts of free Dyn1 protein remaining in the deposition suspension after tubulation were beneficial to balancing adsorption and mobility of the lipid nanotube-Dyn1 assemblies. During imaging, 2 μL of 100 mM GTP was added to the liquid chamber to reach a finial concentration of 1 mM GTP in the solution through a pipette tip gently without disturbing the imaging process. The estimation of GTP diffusion time was conducted by infusing 2 μL of 8-hydroxypyrene-1,3,6-trisulfonic acid, trisodium (HPTS pyranine) to the corner of the HS-AFM liquid chamber. Nominally, it takes ca. 60 s for the GTP to diffuse into the chamber. Prior to the addition of GTP, several movies were captured for each tube.

Formation of Supported Lipid Bilayers (SLBs) on Glass Coverslips. The SLBs were formed by lipid spilling from lipid-covered silica beads as described (31, 48). Briefly, 10 μL of the MLVs suspension prepared as described above was deposited to the bottom of a Petri dish in four equal drops. 1 μL of the 60 μm silica bead suspension (Microspheres-Nanospheres, cat:140264-10) was added to each drop and incubated for 10 min, then the drops were dried by keeping the dish for 15 min under vacuum. MLVs bound to the beads formed dried multilamellar film on the bead surface. To produce the SLB, the lipid-covered beads were picked from the dish bottom with a fire-closed glass capillary and transferred to the observation chamber prefilled with the working buffer. The lipid-covered bead precipitated to the bottom coverslip of the chamber kept at room temperature. While in contact with the coverslip, the beads "spilled" the lipids to the coverslip surface, with large SLB patched forming 10 min after addition of the beads (30, 48). Once the SLBs were formed, the beads were removed via perfusion of the chamber with the working buffer. New lipid-covered beads were subsequently added and rolled over SLB surface to form the NTs.

Formation of the Nanotube Templates for Fluorescence Microscopy Imaging. The NTs were formed by the silica bead "rolling" technique described earlier (31, 48). Using a fire-closed glass capillary, the lipid-covered beads were transferred to the inlet of custom-made microfluidic chamber prefilled with the working buffer. To obtain suspended NTs, we used the chambers with the SU8 micropillar array (5 μm high, 20 μm between the pillars) manufactured on the

bottom coverslip (48). To obtain the NTs attached to the substrate (as in HS-AFM experiments), we used the chamber with the plane coverslip covered by SLB serving to protect the NTs from direct interaction with the glass. The beads were slowly rolled over the bottom of the chamber using a laminar flow. Stable NTs formed between the micropillars (31) or directly over the SLB (*SI Appendix*, Fig. S1D). Proteins and/or nucleotides at the concentrations indicated in the text were applied to the preformed NTs with laminar flow perfusion (30, 31).

High-Speed AFM Imaging. Samples were imaged with an Ando Model high-speed atomic force microscope (RIBM, Japan), equipped with a small cantilever from NanoWorld (Ultra-Short Cantilevers) with a spring constant of $k = 0.15$ N/m and a resonance frequency of $f = 1{,}200$ kHz in water. The microscope was operated in tapping mode at room temperature. An amorphous carbon tip was grown on the top of each cantilever with electron-beam deposition. To minimize the sample disturbance, the free oscillation amplitude was kept between 0.9 and 1.3 nm, and the typical imaging amplitude was set to no less than 85% of the free oscillation amplitude. For the sample stage, a freshly cleaved mica disk with a diameter of 1.5 mm was fixed on a glass rod with a diameter of 1.5 mm and a height of 2 mm using epoxy glue. Before or after the sample stage was fixed with mounting wax on the z-piezo of the HS-AFM scanner, the mica was freshly cleaved. The scanner was then mounted above the sample chamber with a cantilever immersed in GTPase buffer. The typical scan rate was kept at 1 frame per second unless indicated otherwise.

HS-AFM images were converted to 32 bit images by using custom-built Matlab software (49) and processed using the ImageJ software (NIH, Bethesda, MD, USA). Unprocessed versions of the HS-AFM movies are presented as Movies S13–S20. The tilted images were corrected by using Gywddion software (50). The drift of image sequences was corrected with a template matching ImageJ plugin (51). To reduce the noise, all image sequences were processed through a 1×1 median filter. Kymographs were generated by an ImageJ plugin and further analyzed using IgorPro software (WaveMetrix, Lake Oswego, OR, USA). The curvature analysis was adapted from 2D line curvature code (52) and used the following equation:

$$k = \frac{x'y'' - x''y'}{(x'^2 + y'^2)^{3/2}} \quad [1]$$

Fluorescence Microscopy Imaging. The NT interaction with ^{WT}Dyn1-mEGFP and ^{K44A}Dyn1-mEGFP was monitored via an inverted fluorescence microscope (Nikon Eclipse Ti, Japan) with a 100X/1.49NA objective lens and a Zyla 4.2 sCMOS camera (Andor, Ireland) controlled via μManager software (53). CoolLed pE-4000 light source at a low (10%) intensity was used as the epifluorescence excitation source; BrightLine GFP and TRITC filter sets (Semrock) were used for mEGFP and Rh-DOPE fluorescence, respectively. Image processing (background subtraction and kymograph building) and statistical analysis were performed using Fiji package in ImageJ and OriginPro 8.0 software, respectively. The NT radius was measured using the specific Rh-DOPE fluorescence intensity of SLB following the previously developed protocols (30).

Modeling of GTP-Driven Transformation of Dyn1 Helices. Changes of the helical geometry were calculated using Maple 2022 software (MapleSoft) with the helical parameters taken from the cryo-EM analyses of Dyn1 helices (17, 35).

Data, Materials, and Software Availability. Datasets have been deposited in Figshare (DOI: 10.6084/m9.figshare.24759666).

ACKNOWLEDGMENTS. Research reported in this publication was supported by the National Institute of General Medicine of the NIH under award number R01GM121725. The content is solely the responsibility of the authors and does not necessarily represent the official views of the NIH. Work at the Lawrence Livermore National Laboratory was performed under the auspices of the U.S. Department of Energy under Contract DE-AC52-07NA27344. Work at the Molecular Foundry was supported by the Office of Science, Office of Basic Energy Sciences, of the U.S. Department of Energy under Contract No. DE-AC02-05CH11231. The experiments on the fluorescence microscopy analysis of the effects of K44A mutations were partially supported by the Basque Government grant IT1625-22. We thank Julene Ormaetxea Gisasola for the help with Dyn1 GTPase assays.

Author affiliations: [a]Materials Science Division, Physical and Life Sciences Directorate, Lawrence Livermore National Laboratory, Livermore, CA 94550; [b]Biofisika Institute Consejo Superior de Investigaciones Científicas, Universidad del País Vasco, Euskal Herriko Unibersitatea (CSIC, UPV/EHU), University of the Basque Country, Leioa, 48940, Spain; [c]Department of Biochemistry and Molecular Biology, University of the Basque Country, Leioa, 48940, Spain; [d]Ikerbasque, Basque Foundation for Science, Bilbao, 48009, Spain; and [e]School of Natural Sciences, University of California Merced, Merced, CA 93434

Author contributions: V.A.F. and A.N. designed research; Y.Z., J.V.L., M.S.M.A., and P.A. performed research; P.A. contributed new reagents/analytic tools; Y.Z., J.V.L., M.S.M.A., Y.W., V.A.F., and A.N. analyzed data; and Y.Z., M.S.M.A., V.A.F., and A.N. wrote the paper.

The authors declare no competing interest.

This article is a PNAS Direct Submission.

1. S. Watanabe *et al.*, Synaptojanin and endophilin mediate neck formation during ultrafast endocytosis. *Neuron* **98**, 1184 e6–1197 (2018).
2. I. Milosevic, Revisiting the role of clathrin-mediated endoytosis in synaptic vesicle recycling. *Front. Cell. Neurosci.* **12**, 27 (2018).
3. S. M. Ferguson, P. De Camilli, Dynamin, a membrane-remodelling GTPase. *Nat. Rev. Mol. Cell Biol.* **13**, 75–88 (2012).
4. S. L. Schmid, V. A. Frolov, Dynamin: Functional design of a membrane fission catalyst. *Ann. Rev. Cell Dev. Biol.* **27**, 79–105 (2011).
5. G. J. Praefcke, H. T. McMahon, The dynamin superfamily: Universal membrane tubulation and fission molecules? *Nat. Rev. Mol. Cell Biol.* **5**, 133–147 (2004).
6. B. Antonny *et al.*, Membrane fission by dynamin: What we know and what we need to know. *EMBO J.* **35**, 2270–2284 (2016).
7. J. K. Noel, F. Noé, O. Daumke, A. S. Mikhailov, Polymer-like model to study the dynamics of dynamin filaments on deformable membrane tubes. *Biophys. J.* **117**, 1870–1891 (2019).
8. A. Kadosh, A. Colom, B. Yellin, A. Roux, T. Shemesh, The tilted helix model of dynamin oligomers. *Proc. Natl. Acad. Sci. U.S.A.* **116**, 12845–12850 (2019).
9. M. Pannuzzo, Z. A. McDargh, M. Deserno, The role of scaffold reshaping and disassembly in dynamin driven membrane fission. *eLife* **7**, e39441 (2018).
10. M. Fuhrmans, M. Müller, Coarse-grained simulation of dynamin-mediated fission. *Soft Matter* **11**, 1464–1480 (2015).
11. A. V. Shnyrova *et al.*, Geometric catalysis of membrane fission driven by flexible dynamin rings. *Science* **339**, 1433–1436 (2013).
12. J. A. Mears, J. E. Hinshaw, Visualization of dynamins. *Methods Cell Biol.* **88**, 237–256 (2008).
13. M. M. Kozlov, Dynamin: Possible mechanism of "Pinchase" action. *Biophys. J.* **77**, 604–616 (1999).
14. O. Daumke, G. J. Praefcke, Mechanisms of GTP hydrolysis and conformational transitions in the dynamin superfamily. *Biopolymers* **109**, e23079 (2018).
15. V. A. Frolov, A. Escalada, S. A. Akimov, A. V. Shnyrova, Geometry of membrane fission. *Chem. Phys. Lipids* **185**, 129–140 (2015).
16. P. V. Bashkirov *et al.*, GTPase cycle of dynamin is coupled to membrane squeeze and release, leading to spontaneous fission. *Cell* **135**, 1276–1286 (2008).
17. L. Kong *et al.*, Cryo-EM of the dynamin polymer assembled on lipid membrane. *Nature* **560**, 258–262 (2018).
18. A. C. Sundborger *et al.*, A dynamin mutant defines a superconstricted prefission state. *Cell Rep.* **8**, 734–742 (2014).
19. H. Damke, T. Baba, D. E. Warnock, S. L. Schmid, Induction of mutant dynamin specifically blocks endocytic coated vesicle formation. *J. Cell Biol.* **127**, 915–934 (1994).
20. B. D. Song, M. Leonard, S. L. Schmid, Dynamin GTPase domain mutants that differentially affect GTP binding, GTP hydrolysis, and clathrin-mediated endocytosis. *J. Biol. Chem.* **279**, 40431–40436 (2004).
21. J. Liu, F. J. D. Alvarez, D. K. Clare, J. K. Noel, P. Zhang, CryoEM structure of the super-constricted two-start dynamin 1 filament. *Nat. Commun.* **12**, 5393 (2021).
22. J. R. Jimah *et al.*, Cryo-EM structures of membrane-bound dynamin in a post-hydrolysis state primed for membrane fission. *Dev. Cell* **59**, 1783–1793 (2024).
23. E. Cocucci, R. Gaudin, T. Kirchhausen, Dynamin recruitment and membrane scission at the neck of a clathrin-coated pit. *Mol. Biol. Cell* **25**, 3595–3609 (2014).
24. A. Grassart *et al.*, Actin and Dynamin2 dynamics and interplay during clathrin-mediated endocytosis. *J. Cell Biol.* **205**, 721–735 (2014).
25. T. Takeda *et al.*, Dynamic clustering of dynamin-amphiphysin helices regulates membrane constriction and fission coupled with GTP hydrolysis. *eLife* **7**, e30246 (2018).
26. A. Colom, L. Redondo-Morata, N. Chiaruttini, A. Roux, S. Scheuring, Dynamic remodeling of the dynamin helix during membrane constriction. *Proc. Natl. Acad. Sci. U.S.A.* **114**, 5449–5454 (2017).
27. S. Morlot *et al.*, Membrane shape at the edge of the dynamin helix sets location and duration of the fission reaction. *Cell* **151**, 619–629 (2012).
28. J. Fierling, A. Johner, I. M. Kulić, H. Mohrbach, M. M. Müller, How bio-filaments twist membranes. *Soft Matter* **12**, 5747–5757 (2016).
29. S. Dar, S. C. Kamerkar, T. J. Pucadyil, A high-throughput platform for real-time analysis of membrane fission reactions reveals dynamin function. *Nat. Cell Biol.* **17**, 1588–1596 (2015).

30. S. Dar, S. C. Kamerkar, T. J. Pucadyil, Use of the supported membrane tube assay system for real-time analysis of membrane fission reactions. *Nat. Protoc.* **12**, 390–400 (2017).
31. I. Pérez-Jover *et al*., Allosteric control of dynamin-related protein 1 through a disordered C-terminal short linear motif. *Nat. Commun.* **15**, 52 (2024).
32. T. Ando *et al*., A high-speed atomic force microscope for studying biological macromolecules. *Proc. Natl. Acad. Sci. U.S.A.* **98**, 12468–12472 (2001).
33. T. Ando, T. Uchihashi, S. Scheuring, Filming biomolecular processes by high-speed atomic force microscopy. *Chem. Rev.* **114**, 3120–3188 (2014).
34. A. Roux, K. Uyhazi, A. Frost, P. De Camilli, GTP-dependent twisting of dynamin implicates constriction and tension in membrane fission. *Nature* **441**, 528–531 (2006).
35. P. Zhang, J. E. Hinshaw, Three-dimensional reconstruction of dynamin in the constricted state. *Nat. Cell Biol.* **3**, 922–926 (2001).
36. J. Espadas *et al*., Dynamic constriction and fission of endoplasmic reticulum membranes by reticulon. *Nat. Commun.* **10**, 5327 (2019).
37. V. Galli *et al*., Uncoupling of dynamin polymerization and GTPase activity revealed by the conformation-specific nanobody dynab. *eLife* **6**, e25197 (2017).
38. M. H. Stowell, B. Marks, P. Wigge, H. T. McMahon, Nucleotide-dependent conformational changes in dynamin: Evidence for a mechanochemical molecular spring. *Nat. Cell Biol.* **1**, 27–32 (1999).
39. D. A. Zacharias, J. D. Violin, A. C. Newton, R. Y. Tsien, Partitioning of lipid-modified monomeric GFPs into membrane microdomains of live cells. *Science* **296**, 913–916 (2002).
40. X. Cheng *et al*., Dynamin-dependent vesicle twist at the final stage of clathrin-mediated endocytosis. *Nat. Cell Biol.* **23**, 859–869 (2021).
41. P. Bassereau *et al*., The 2018 biomembrane curvature and remodeling roadmap. *J. Phys. D Appl. Phys.* **51**, 343001 (2018).
42. Y. Kozlovsky, M. M. Kozlov, Membrane fission: Model for intermediate structures. *Biophys. J.* **85**, 85–96 (2003).
43. J. P. Mattila *et al*., A hemi-fission intermediate links two mechanistically distinct stages of membrane fission. *Nature* **524**, 109–113 (2015).
44. M. Simunovic *et al*., Friction mediates scission of tubular membranes scaffolded by BAR proteins. *Cell* **170**, 172–184 (2017).
45. K. Aftahy *et al*., Molecular sensing and manipulation of protein oligomerization in membrane nanotubes with bolaamphiphilic foldamers. *J. Am. Chem. Soc.* **145**, 25150–25159 (2023).
46. N. Mehrotra, J. Nichols, R. Ramachandran, Alternate pleckstrin homology domain orientations regulate dynamin-catalyzed membrane fission. *Mol. Bio. Cell* **25**, 879–890 (2014).
47. D. A. Ramirez-Diaz *et al*., FtsZ induces membrane deformations via torsional stress upon GTP hydrolysis. *Nat. Commun.* **12**, 3310 (2021).
48. J. M. M. Galvez, M. Garcia-Hernando, F. Benito-Lopez, L. Basabe-Desmonts, A. V. Shnyrova, Microfluidic chip with pillar arrays for controlled production and observation of lipid membrane nanotubes. *Lab Chip* **20**, 2748–2755 (2020).
49. Y. Zhang, R. H. Tunuguntla, P. O. Choi, A. Noy, Real-time dynamics of carbon nanotube porins in supported lipid membranes visualized by high-speed atomic force microscopy. *Phil. Trans. R. Soc. B Biol. Sci.* **372**, 20160226 (2017).
50. D. Nečas, P. Klapetek, Gwyddion: An open-source software for SPM data analysis. *Open Phys.* **10**, 181–188 (2012).
51. Q. Tseng *et al*., A new micropatterning method of soft substrates reveals that different tumorigenic signals can promote or reduce cell contraction levels. *Lab Chip* **11**, 2231–2240 (2011).
52. D. J. Kroon, 2D line curvature and normals. MATLAB Central File Exchange (2011). https://www.mathworks.com/matlabcentral/fileexchange/32696-2d-line-curvature-and-normals. Accessed 3 June 2019.
53. A. Edelstein, N. Amodaj, K. Hoover, R. Vale, N. Stuurman, Computer control of microscopes using μManager. *Curr. Protoc. Mol. Biol.* **92**, 14.20.1–14.20. 17 (2010).